A small-angle neutron scattering and transmission electron microscopy study of krypton precipitates in copper

1996 J. Phys.: Condens. Matter 8 8431

(http://iopscience.iop.org/0953-8984/8/44/001)

J. Phys.: Condens. Matter **8** (1996) 8431–8455. Printed in the UK

A small-angle neutron scattering and transmission electron microscopy study of krypton precipitates in copper

Jan Skov Pedersen†, Andy Horsewell‡ and Morten Eldrup‡

† Department of Solid State Physics, Risø National Laboratory, DK-4000 Roskilde, Denmark
‡ Materials Department, Risø National Laboratory, DK-4000 Roskilde, Denmark

Received 19 April 1996, in final form 4 September 1996

Abstract. The annealing behaviour of bulk copper containing 2.6 at.% krypton has been studied by small-angle neutron scattering (SANS) and transmission electron microscopy (TEM). In addition positron annihilation spectroscopy (PAS) and mass-density measurements (MDM) were made. In the as-prepared and annealed material a high density of krypton precipitates ('bubbles') exists. Special emphasis is put on different approaches to the analysis of the SANS data. Differences between the results from the various analyses are pointed out and discussed. Polydisperse models clearly give the most extensive information, i.e. the size distribution of the Kr bubbles and integral parameters derived from it (i.e. bubble volume, total surface area and average radius). It is demonstrated that a correct choice of form factor is important for the reliability of the derived size distribution. In TEM a high degree of overlap of bubble images is observed and corrected for. Good agreement between the shapes of SANS and TEM size distributions is found, while differences in amplitude are ascribed to experimental uncertainties. Average krypton densities in the bubbles as well as fractional cavity volumes derived from PAS and MDM are found to be in good agreement, but the cavity volumes are clearly larger than the total bubble volumes obtained from the SANS and TEM size distributions. Above roughly 300 °C bubble growth takes place. Two different mechanisms for the initiation of growth are discussed. At the higher annealing temperatures the growth in bubble size and total volume fraction is explained by bubble migration and coalescence followed by absorption of thermal vacancies.

1. Introduction

The behaviour of inert-gas atoms in metals is to a large extent dominated by their extremely low solubility which provides a high probability for the formation of gas precipitates, so-called gas bubbles. There is an ongoing interest in studies of inert-gas behaviour in materials for applications (e.g. fusion technology, nuclear fuels, materials modifications) and from a more fundamental viewpoint (e.g. Ullmaier 1983, Donnelly and Evans 1991).

In order to try to obtain a full picture of the microstructural parameters, such as bubble concentrations, size distributions, and gas densities, it is useful to combine different experimental techniques (Donnelly 1985). Such a combined approach also allows the techniques themselves to be monitored, especially with regard to the mutual consistency of the results that they provide. Previously, this route was taken in an experimental study into the annealing behaviour of Cu and Ni containing percentage concentrations of krypton (Jensen *et al* 1988), using the techniques of positron annihilation spectroscopy (PAS), transmission electron microscopy (TEM) and scanning electron microscopy (SEM) together with weight and dimension measurements. In the present paper we shall discuss

0953-8984/96/448431+25$19.50

investigations of the annealing behaviour of Kr bubbles in Cu primarily by small-angle neutron scattering (SANS) and TEM. The main emphasis will be on the SANS measurements and data analysis, partly in order to obtain complementary information to the TEM bubble size distributions, but also to study the problems involved in detailed analyses of SANS data for samples containing a high concentration of polydisperse precipitates.

Studies using SANS normally require bulk samples, so the usual methods of inducing relatively thin layers of high concentrations of inert gases into metals by ion implantation (Schwahn *et al* 1983, Qiang-Li *et al* 1990) are not ideally suited. However, here, as in the previous studies, we have utilized the bulk samples of copper containing 2.6 at.% Kr prepared at Harwell, UK, by a combined sputter/implantation technique that produces centimetre thick specimens (Whitmell 1981, Whitmell *et al* 1983). Previous work on material prepared in this way has established that the substructure in the as-prepared condition consists of very small grains (a few tenths of micrometres) containing a high density of small bubbles with diameters of 30 Å and smaller. A high dislocation density was another feature of the substructure. Electron diffraction studies showed that the Kr in the bubbles is in a crystalline state (Evans and Mazey 1985) and it was argued (Eldrup and Evans 1982, Evans *et al* 1985) that only the larger bubbles were seen in TEM, while a considerable fraction (up to 75%) of the Kr was present in submicroscopic bubbles or vacancy–Kr clusters. It has been established that, on annealing above approximately 400 °C, the solid Kr melts, the bubbles begin to migrate and grow, and a grain boundary bubble population develops. The average Kr density in the bubbles decreases due to an increased total bubble volume, and eventually (at 600–700 °C) an extreme swelling of the Cu–Kr material takes place with a simultaneous release to the surface of a major fraction of the krypton (Evans *et al* 1985, Williamson 1985, Jensen *et al* 1988).

The previous investigations by TEM, SEM and PAS were made on samples which were similarly, but not identically, prepared and annealed. To make a more direct comparison, the samples for the present study were therefore cut side-by-side from the same piece of material and annealed in precisely the same way. Both SANS, TEM and PAS studies have been carried out on these specimens, emphasizing the SANS. We have used analysis methods of increasing complexity for the SANS data, starting with model-independent methods (section 3.1) and thereafter using models that include assumptions about monodispersity of the krypton bubbles (section 3.2). In the final steps of complexity, polydisperse models are used and size distributions of bubbles are determined (section 3.3), using both a model that neglects inter-bubble correlation effects and a model that includes these. All of the analyses are done on an absolute intensity scale and thus give parameters such as volume fractions and concentrations of bubbles.

The paper is organized in the following way. Section 2 describes some experimental details. In section 3 a discussion of the SANS data analysis and results are given, while in section 4 the TEM results are presented. In section 5 additional results from other experiments are described and section 6 contains a discussion, including a comparison between the different techniques and with previous studies. Finally, a brief summary and some conclusions are given in section 7.

2. Experimental details

2.1. The samples

The sample material, consisting of copper containing a high concentration of krypton, was produced by the Harwell combined sputtering/implantation technique (Whitmell 1981,

Whitmell *et al* 1983, Williamson 1985). On the macroscopic scale the material had a clearly layered structure reflecting some inhomogeneity in the deposition of Cu and Kr (Williamson 1985). An average content of 2.6% Kr was measured for the present specimen (section 5). The SANS sample was a $10\times10\times1.45$ mm^3 plate, cut with its major surfaces perpendicular to the surface of the deposited Cu layers. SANS measurements were carried out (at room temperature) on this specimen, in the as-prepared state and after vacuum annealing (at about 2×10^{-6} Torr) to each of the temperatures 275 °C, 425 °C and 575 °C. The holding time was 30 min at each temperature. Throughout this paper we denote the as-prepared sample AP, and the annealed samples A275, A425, and A575, respectively.

The TEM samples were prepared by cutting, side-by-side with the SANS sample, 0.5 mm thick slices from the bulk material; slices were cut both parallel and perpendicular to the deposited layers. Discs of diameter 3 mm were punched from the slices and annealed in the same way as the SANS sample, providing sets of samples annealed to the same temperature. After annealing, the discs were carefully ground by hand to a thickness of 0.15 mm. Finally, the specimens were twin-jet electropolished to electron transparency using 20% HNO_3 in methanol at room temperature. To avoid surface oxidation, the foils were immediately transferred to the TEM for examination.

2.2. Small-angle neutron scattering

The experiments were performed on the 12 m small-angle neutron scattering facility at Risø National Laboratory, Denmark (Lebech 1990, Juul Jensen *et al* 1992). The neutrons are monochromatized by a mechanical velocity selector with a relative wavelength resolution of $\Delta\lambda/\lambda = 0.18$. The collimation is determined by a source aperture of 16 mm and a sample aperture of 8 mm in diameter. The distance L between the apertures can be varied between 1 and 6 m and the distance l between the sample and the detector can also be varied from 1 to 6 m. The scattered neutrons are detected by an area-sensitive detector divided into 128×128 pixels, with a spatial resolution of 0.8 cm (full-width–half-maximum value).

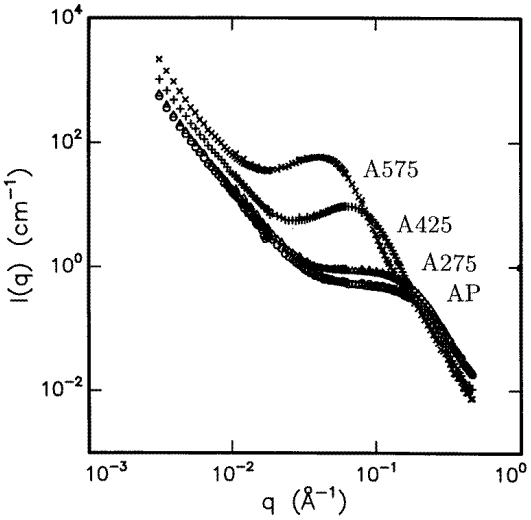

Figure 1. The measured small-angle scattering data for the as-prepared sample (AP) and the samples annealed to 275 °C (A275), 425 °C (A425), and 575 °C (A575).

The SANS spectra were collected for the following four instrument settings: (L = 3 m, l = 1 m) and $L = l$ = 3 m both for the wavelength λ = 3.22 Å, $L = l$ = 3 m for λ = 8.88 Å and $L = l$ = 6 m for λ = 15.3 Å. This covers a total range of scattering vectors q from 0.002 Å^{-1} to 0.5 Å^{-1}. The measured spectra were corrected according to standard procedures for background, as measured with an empty sample holder, and for electronic noise and room background, as measured with boronated plastic in the sample holder (see e.g. Abis *et al* 1990). The data were, by means of a standard water sample, corrected for detector efficiency and put on absolute scale (Wignall and Bates 1987). The incoherent scattering (0.0075 cm^{-1}) from the copper matrix was also subtracted.

The radially averaged spectra are displayed in figure 1 in a double-logarithmic representation. For all annealing temperatures the spectrum has an approximate q^{-3}-behaviour at small scattering vectors. At larger scattering vectors the radially averaged spectra have a peak or a shoulder which moves to smaller scattering vectors and increases in intensity for increasing annealing temperatures. We associate the latter feature with the krypton bubbles and their increase in size upon annealing. The two-dimensional scattering patterns of the scattering from the bubbles are nearly isotropic except for the spectrum for A575 which has a weak anisotropy with sixfold symmetry.

2.3. Transmission electron microscopy

Specimens were observed in a JEOL 2000FX transmission electron microscope operating at 200 keV. The specimens were mounted in a eucentric double-tilt holder, which allows single regions of the thin foil to be observed after tilting (for diffraction contrast experiments) about two orthogonal tilts of up to $\pm 35^\circ$.

The regions of the foil chosen for observation and analysis were generally 100–200 Å thick. The krypton precipitates were observed by applying standard diffraction contrast and mass-thickness contrast techniques. Using these techniques, and operating the microscope to obtain the optimum point-to-point resolution of 2.4 Å, precipitates could be distinguished down to 7–8 Å in diameter. Observation was carried out at a working magnification of 2×10^5, and size distributions were determined by direct manual measurement using prints with a total magnification of 1×10^6.

3. SANS data: analysis and results

As mentioned in the introduction we have used methods of increasing complexity in the analysis of the SANS data. This is done in order to investigate the problems involved with detailed data analysis of small-angle scattering data for polydisperse systems with high concentrations of precipitates. In the following we start by describing the low-q power-law scattering. Secondly, we use the method of indirect Fourier transformation (Glatter 1977) to obtain the distance distribution (correlation) function of the bubbles and to subtract the power-law scattering from the measured spectra. The average bubble size can be estimated from the correlation function. Then we shall use the Porod expression (Porod 1982) for determining the total surface area of the bubbles from the high-q part of the data, and next apply the general two-phase model (Porod 1982) for the determination of the bubble volume fraction (section 3.1). In section 3.2, monodisperse models are presented. First a two-shell model is used for interpreting the distance distribution function and secondly a monodisperse hard-sphere model is applied. In the polydisperse models (section 3.3) a form-free expression is used for the size distribution (Glatter 1980). In the first part of the analysis only the high-q part of the data, which is free of the inter-bubble correlation effects,

is used. In the final analysis we include the correlation effects in the 'local monodisperse approximation' (Pedersen 1994).

In the present work the instrumental resolution was included in the analysis following Pedersen *et al* (1990) and Pedersen (1993a). The instrumentally smeared cross section $I(\langle q\rangle)$ is given by

$$I(\langle q\rangle) = \int R(\langle q\rangle, q)\frac{\mathrm{d}\sigma}{\mathrm{d}\Omega}(q)\ \mathrm{d}q \tag{1}$$

where $\langle q\rangle$ is the nominal scattering vector, and $\mathrm{d}\sigma(q)/\mathrm{d}\Omega$ is the ideal non-smeared cross section. $R(\langle q\rangle, q)$ is the resolution function, describing the distribution of neutrons with scattering vectors q, being detected with the nominal scattering vector $\langle q\rangle$.

3.1. Model-independent information

The first step of the analysis concerns the power-law scattering observed at small scattering vectors. The following empirical expression was fitted at small scattering vectors ($q < 0.02$–0.03 Å^{-1}, depending on the sample):

$$\frac{\mathrm{d}\sigma}{\mathrm{d}\Omega}(q) = A_1 q^{-A_2} + A_3 \tag{2}$$

where A_i are fitting parameters. The fits gave the power $A_2 = 2.87 \pm 0.01$ for the samples AP, A275, and A425, and $A_2 = 3.276 \pm 0.003$ for A575.

The neutron wavelength of 3.22 Å used for sample–detector distances of 1 m and 3 m was chosen due to flux considerations. However, this turned out to be unfavourable since the short wavelength gives rise to double Bragg scattering (Warren 1959). Therefore the sample A575 was later remeasured at 3.0 Å and 6.0 Å. The double Bragg scattering was determined as the difference between the 3.0 Å and 6.0 Å data. The contribution was subtracted from all of the data measured for 3.22 Å.

Direct spatial information on the bubble sizes and correlations can be obtained by the indirect Fourier transformation (IFT) method of Glatter (1977). By this method the distance distribution function

$$p(r) = r^2 \int \rho(\boldsymbol{r}')\rho(\boldsymbol{r}' + \boldsymbol{r})\ \mathrm{d}\boldsymbol{r}' \tag{3}$$

where $\rho(\boldsymbol{r})$ is the excess scattering length density, is determined. The cross section of a sample with isotropic scattering is the Fourier transform of $p(r)$:

$$\frac{\mathrm{d}\sigma}{\mathrm{d}\Omega}(q) = 4\pi \int p(r)\frac{\sin(qr)}{qr}\ \mathrm{d}r. \tag{4}$$

$p(r)$ is expressed by a linear combination of cubic b-spline functions (Glatter 1977) and the coefficients determined by fitting (4), smeared by instrumental resolution, to the experimental data.

The power-law scattering at low q is not expected to originate from the Kr bubbles as no bubbles of large size are observed by TEM. In order to subtract the contribution from the scattering we modified the IFT method to include the term q^{-A_2} with a scale factor as a fitting parameter. The $p(r)$-functions, thus determined, are shown in figure 2. They give an estimate of the typical sizes of the bubbles as the first peak in $p(r)$ is the bubble self-correlation peak. For a solid sphere, $p(r)$ has a maximum close to the radius R of the sphere and $p(r)$ goes to zero at $2R$. Thus, the self-correlation peak suggests radii of about 12 Å for the AP and A275 samples, 20 Å for A425, and 40 Å for A575. The negative values of $p(r)$ arise from depletion of Kr in a region outside a bubble. The

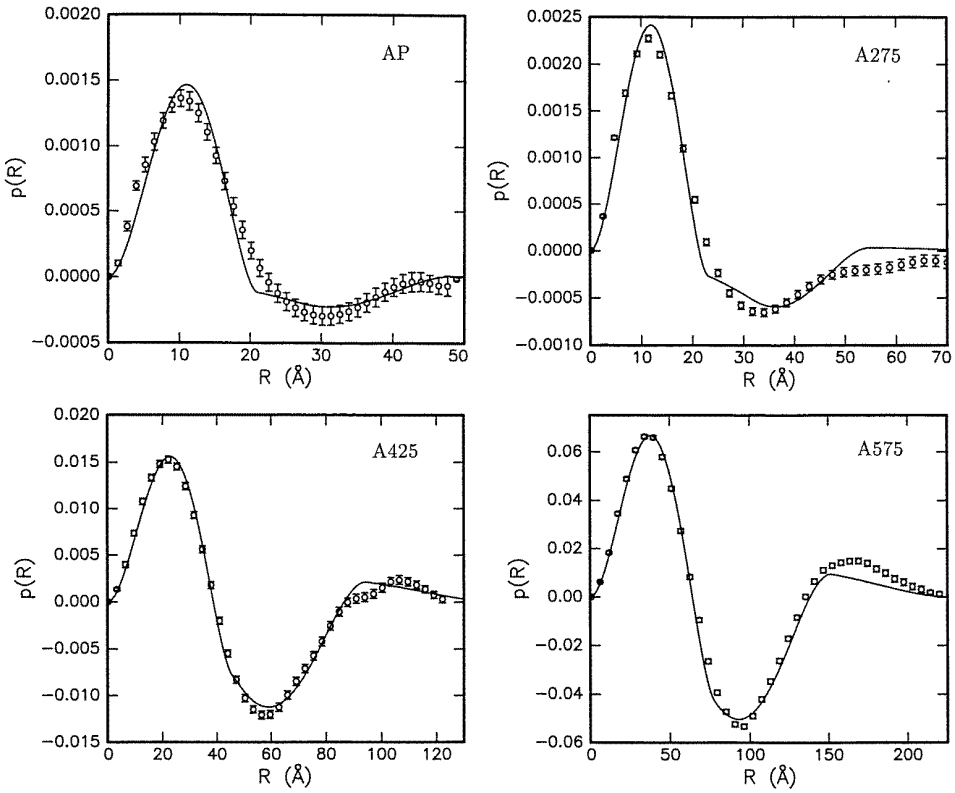

Figure 2. Distance distribution functions $p(r)$. The points are from the indirect Fourier transformation and the curves are the fits with the two-shell model.

Table 1. Bubble volume fractions V obtained from the SANS data using three different models, i.e. the two-phase model, the two-shell model and the monodisperse hard-sphere model. The scattering contrast $\Delta\rho$ between the bubbles and the Cu matrix is given. The specific surface area S was calculated from fits of the Porod expression.

	$\Delta\rho$ (10^{10} cm^{-2})	S (Porod) (10^6 cm^{-1})	V (two phase)	V (two shell)	V (hard sphere)
AP	4.64	1.75	0.023	0.025	0.022
A275	4.74	1.70	0.030	0.033	0.029
A425	4.90	0.96	0.052	0.056	0.048
A575	5.29	0.65	0.075	0.083	0.063

effective scattering density is obtained as scattering due to Kr bubbles minus the average scattering density of the sample (Cu + Kr). As Kr and Cu have effective scattering length densities of opposite sign, a depleted region outside the bubbles will give rise to a negative value of $p(r)$. For A425 and A575, $p(r)$ has a positive peak at large r-values, indicating bubble–bubble correlation. Note that the data sets used in the rest of the analysis have the power-law scattering subtracted (see figure 4, later).

The Porod law

$$\frac{d\sigma}{d\Omega}(q) = 2\pi S \Delta\rho^2 q^{-4} \tag{5}$$

which is valid for large q, can be used for model-independent determination of the specific surface area S. $\Delta\rho$ is the difference in scattering length density between the bubbles and Cu matrix. $\Delta\rho$ (table 1) has been calculated from the Kr densities determined by positron annihilation measurements (Jensen *et al* 1988). The specific surface area (table 1), determined using (5), decreases by about a factor of three on annealing.

In the approximation of a 'two-phase model' (Porod 1982), the volume fraction of the Kr bubbles can be derived from the 'invariant':

$$Q = \int_0^\infty \frac{d\sigma}{d\Omega}(q) q^2 \, dq \tag{6}$$

which is related to the volume fraction V of the bubbles:

$$Q = \Delta\rho^2 V(1 - V) 2\pi^2. \tag{7}$$

The invariant Q was calculated using the Fourier transform of $p(r)$ determined from IFT as this reduces the influence of instrumental resolution effects. Beyond q = 0.5 Å^{-1} the scattering curves were extrapolated as q^{-4}. The volume fractions determined from Q (table 1: 'two-phase') is found to increase by about a factor of three from the AP sample to the A575 sample.

The volume fraction V and the surface area S, determined from the Porod fit can be used for determining an (average) radius: $\overline{R} = 3V/S$. The values determined by this relation are: 3.9 Å, 5.3 Å, 16 Å and 34 Å for increasing annealing temperatures. These values are quite different from those estimated from $p(r)$, especially for the AP and A275 sample, for which they differ by more than a factor of two. These differences are likely to be due to the application of the Porod expression (5) at scattering vectors smaller than where it is valid. This shows that the results from such a simple analysis should be considered with caution.

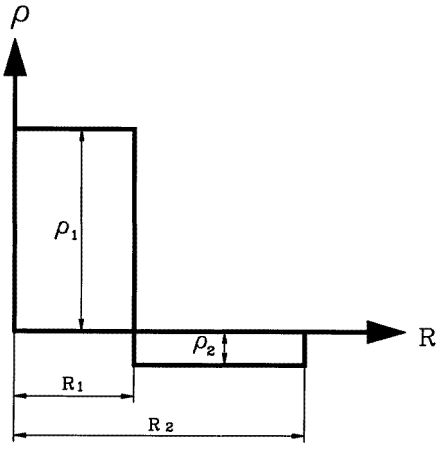

Figure 3. A schematic representation of the two-shell model.

Table 2. Parameters from the two-shell model applied to SANS data (see figure 3). N_B is the bubble density. The scattering contrast $\Delta\rho'$ used for bubbles relative to the average scattering length density of the samples is given. The fitted parameters R_1 and R_2 are the radii of the two shells, and ρ_1 and ρ_2 are the relative scattering length densities.

	$\Delta\rho'$ (10^{10} cm^{-2})	R_1 (Å)	R_2 (Å)	R_2/R_1	ρ_1 (10^{19} cm$^{-5/2}$)	ρ_2 (10^{17} cm$^{-5/2}$)	$-\rho_2/\rho_1$ (10^{-3})	N_B (10^{18} cm^{-3})
AP	4.09	10.5	37.7	3.59	9.35	−2.98	3.19	5.23
A275	4.18	11.6	43.2	3.72	9.4	−4.43	4.71	5.06
A425	4.26	22.9	71.9	3.14	4.50	−9.92	22.0	1.11
A575	4.43	38.7	114.0	2.93	2.59	−6.79	26.2	0.34

3.2. Monodisperse models

The distance distributions from IFT can be converted to actual scattering length density distributions (Glatter 1981). The negative parts of $p(r)$ (figure 2) suggest that a shell model with at least two shells is required for the scattering length density $\rho(\boldsymbol{r})$, in order to describe the distance distribution function. A schematic drawing of this model is shown in figure 3. The model has four parameters: two radii R_1 and R_2, and two parameters ρ_1 and ρ_2 proportional to the scattering length density of the two shells. It can be shown that $\rho_1 = \sqrt{N_B}\,\Delta\rho'$, where N_B is the number density of bubbles and $\Delta\rho'$ is the scattering length density of the bubbles, relative to the average scattering density of the sample. Table 2 contains $\Delta\rho'$ calculated using the Kr densities determined by positron annihilation measurements (Jensen *et al* 1988) and the estimated Kr concentration of 2.6%.

The fits to the $p(r)$-functions were reasonable for this two-shell model. They are shown as full lines in figure 2 and the corresponding parameters are displayed in table 2. The radii of the inner shell agree with those estimated from the shape of the bubble self-correlation peak in $p(r)$. The radius of the outer shell (the Kr-depleted layer) is about 3–4 times larger than the radius of the bubble. The values for ρ_1 and $\Delta\rho'$ were used to calculate the bubble concentrations according to $N_B = \rho_1^2/\Delta\rho'^2$ (table 2). The values decrease about a factor of 15 from the AP sample to the A575 sample. The volume fractions calculated from N_B and R_1 agree within 10% with the values found by the two-phase model (table 1). The onset of bubble growth (increase in R_1) and onset of change in bubble volume occurs at approximately 300 °C (tables 1 and 2). At this point the ratio $|\rho_2/\rho_1|$ increases by about a factor of eight. Since it is known from PAS (Jensen *et al* 1988) that the change in ρ_1 is small this shows that the krypton depletion just outside a bubble becomes more pronounced.

The two-shell model is a low-resolution interpretation of the data in real space and it does not give a perfect fit to the $p(r)$-functions. The two main reasons for the deviations are the polydispersity in the size of the bubbles and the quite crude approximation used for describing the inter-bubble correlation effects. The model neglects that the neighbourhood of a bubble is to some extent structured, as it contains other bubbles. Both of these effects are taken into account in the models in the next section.

The traditional approach for analysing small-angle scattering data is to perform model fits directly to the scattering curves. The scattering curve is, at small q-values, dominated by the scattering from the large particles. Thus, when fitting monodisperse models to the data from a polydisperse system, these will mainly mimic the scattering from the large particles. However, the polydispersity of the particles will show up at large q-values. Consequently, the monodisperse models have to be considered as low-resolution models, and one is forced to restrict the fits to small q-values. The most common approach is to fit the well known

Guinier expression (Guinier and Fournet 1955) to the data in order to obtain the radius of gyration R_g of the particles. However, this expression is only valid for a very dilute system without inter-particle correlation effects. One could instead use the two-shell model and fit the Fourier transform directly to the data. We have done this, and as expected, identical results to those found by fitting the two-shell model to $p(r)$ are obtained.

The two-shell model takes into account the correlation effects in a very crude way. Bubbles that are very close will clearly coalesce and this gives a certain physically determined minimum distance between the bubbles. Next, we will therefore assume that the configuration of the bubbles can be approximated by that of a collection of particles interacting with a hard-spheres potential. Such a model was introduced by Laslaz *et al* (1977) for analysing the small-angle scattering from precipitates in alloys. In the hard-sphere model we assume an interaction radius R_{HS} which is larger than the radius R of the bubble. The cross section is

$$\frac{\mathrm{d}\sigma}{\mathrm{d}\Omega}(q) = N_B\,\Delta\rho^2\,\Phi(q,R)^2\,S(q) \tag{8}$$

where $\Phi(q, R)$ is the form factor of a solid sphere:

$$\Phi(q,R) = 3V_0[\sin(qR) - qR\,\cos(qR)]/(qR)^3 \tag{9}$$

and V_0 is the volume of the sphere with radius R. The term $S(q)$ is the structure factor describing the interference effects. Expressions for $S(q)$ calculated in the Percus–Yevick approximation can be found in Pedersen (1994).

Table 3. Parameters obtained by fitting the monodisperse hard-sphere model to the SANS data. The parameter R is the bubble radius, R_{HS} the hard-sphere radius, η the hard-sphere volume fraction, and N_B the bubble density.

	R (Å)	η	R_{HS}/R	N_B (10^{18} cm^{-3})
AP	10.3	0.037	2.00	4.84
A275	11.1	0.063	2.18	5.12
A425	22.1	0.173	1.81	1.07
A575	37.1	0.169	1.73	0.294

The model was fitted for $q < 0.3$ Å^{-1}, 0.25 Å^{-1}, 0.175 Å^{-1} and 0.10 Å^{-1} for the samples AP, A275, A425, and A575, respectively. The parameters from the fits are given in table 3. The radii of the bubbles agree very well with those determined by fitting the two-shell model to $p(r)$. The ratio R_{HS}/R follows closely the temperature dependence of the ratio of the two radii in the two-shell model. The hard-sphere volume fractions (η) are quite small; calculating the bubble volume fraction from $V = \eta\,(R/R_{HS})^3$ gives values which are much smaller than found from the two-phase model and the two-shell model. However, a calculation of V from the bubble concentrations and the radii determined by the fit gives values which are in good agreement with the two other models (table 1).

3.3. Polydisperse models

In the models used in the previous section we have used monodisperse models which were not able to fit the scattering data at large scattering vectors. This is due to the polydispersity of the bubbles, which, in the scattering intensity, gives rise to a smearing of the oscillations originating from the form factor (9). In the present section we shall analyse the data using polydisperse models.

3.3.1. Dilute systems. First we apply a model which does not take into account the effects of correlation between the bubbles. For a sample consisting of a dilute collection of bubbles, the scattering total cross section is the sum of the scattering of the individual bubbles. By introducing the number size distribution $N(R)$, which is defined as the number of bubbles with radius between R and $R + \mathrm{d}R$, the cross section can be written as

$$\frac{\mathrm{d}\sigma}{\mathrm{d}\Omega}(q) = \Delta\rho^2 \int_0^\infty N(R)\Phi(q, R)^2 \, \mathrm{d}R \tag{10}$$

in which $\Phi(q, R)$ is the form factor of the spherical bubble (9) and $\Delta\rho$ is assumed to be independent of size. The size distribution $N(R)$ was expressed as a linear combination of cubic b-spline functions, the coefficients of which were determined by a constrained least-squares method as described by Glatter (1980) and Pedersen (1994).

As mentioned, equation (10) is only valid for dilute samples, for which inter-particle correlation effects can be neglected. Inter-bubble correlation effects mainly influence the part of the scattering curve at small scattering vectors (see e.g. Glatter 1979). Therefore equation (10) was only fitted to the large-q part of the scattering curves. The ranges were $q > 0.1$ Å^{-1} for the AP and A275 samples, $q > 0.08$ Å^{-1} for A425, and $q > 0.05$ Å^{-1} for A575. (A similar approach was used by Abis *et al* (1990) for precipitates in an Al–Li alloy).

Table 4. Volume fractions V, specific surface area S and weighted average radius R_{Av} as derived from the size distributions. (I) Bubble correlation effects not included. (II) Bubble correlation effects included in the local monodisperse model. (III) Volume fraction calculated from R_{HS}/R and η.

	V			S (10^6 cm^{-1})		R_{Av} (Å)		R_{HS}/R
	I	II	III	I	II	I	II	II
AP	0.029	0.030	0.041	1.11	1.06	8.4	12.7	1.22
A275	0.037	0.036	0.017	1.24	1.19	11.5	13.2	1.73
A425	0.060	0.057	0.057	0.88	0.87	26.8	26.2	1.58
A575	0.076	0.072*	0.097	0.61	0.66*	46.4	48.6*	1.35

* Octahedra for $R > 40$ Å.

The size distributions determined for the four annealing steps are displayed as broken lines in figure 5 (see later). The size distributions for the AP and A275 samples were defined by seven splines in the interval [0; 20 Å]. The distributions are broad with the major component in the region 0–11 Å. A much smaller secondary component of large bubbles is observed at around 14 Å. This portion of the distribution is influenced by the correlation effects which might be present at the smaller q-values in the fitted ranges, and therefore the feature is probably not significant. For the A425 sample, the size distribution, defined by 10 splines in [0; 40 Å], is bimodal with one component at around 7 Å and another at around 20 Å. For this sample there is again a small feature present at large R-values (30 Å). For the A575 sample the distribution was defined by 10 splines in the interval [0; 70 Å]. For this sample the distribution is again bimodal with a component at around 10 Å and one at around 35 Å. In order to check the significance of the component at around 10 Å for the A575 sample a second fit was performed using 10 splines in the interval [10; 80 Å] (i.e., the distribution is set equal to zero below 10 Å). The agreement between the model and the experimental data was estimated by the mean squared residual (MSR) (see e.g. Glatter 1977). It was 19.1 for the interval [10; 80 Å] compared to 7.7 for the interval

[0; 70 Å], which shows that the component of small bubbles is a statistically significant feature of the size distribution. The size distribution as determined by transmission electron microscopy (TEM) (section 4) did not have the component at around 10 Å and it is therefore relevant to consider possible systematic errors which influence the distributions determined by small-angle scattering. The increase in MSR comes mainly from the points at large q-values in the measured data, where the model scattering curve for [10; 80 Å] lies below the measured data. The scattering in this (Porod) region is proportional to q^{-4} times the total surface area of the particles and the discrepancies show that the model surface area is too low. This could be due to the particles having deviations from the assumed spherical shape. In order to fit the data better at large q-values, the bubbles should have a form which has a larger surface area relative to the radius of gyration R_g. In fact the TEM observations show faceting of the largest bubbles which does give rise to a larger surface-to-R_g ratio. We will return to the question later in this section.

The volume fraction and specific surface area can be calculated from the size distributions according to

$$V = \int_0^\infty \frac{4}{3}\pi R^3 N(R)\ \mathrm{d}R \tag{11}$$

$$S = \int_0^\infty 4\pi R^2 N(R)\ \mathrm{d}R. \tag{12}$$

The values for V and S are given in table 4, and agree very well with those determined from the two-phase model (table 1) and the monodisperse models. The S-values differ significantly from those determined by the fit at high q-values of the Porod expression (table 1). This means, that the Porod analysis was performed outside the range of validity leading to an overestimation of S and hence to too low values of the radii ($\overline{R} = 3V/S$) as mentioned earlier.

For polydisperse systems the radius of gyration R_g is given by (Baur and Gerold 1964)

$$R_g^2 = 3\overline{R^8}/5\overline{R^6} \tag{13}$$

where

$$\overline{R^n} = \int_0^\infty R^n N(R)\ \mathrm{d}R \Big/ \left(\int_0^\infty N(R)\ \mathrm{d}R\right). \tag{14}$$

In accordance with this we define an average radius:

$$R_{Av} = \sqrt{\overline{R^8}/\overline{R^6}} \tag{15}$$

which can be compared to the radii determined using the monodisperse models. The values are given in table 4. A comparison with R_1 in table 2 from the two-shell model and R in table 3 from the monodisperse hard-spheres model shows that the values agree within 20%.

3.3.2. Dense systems. In order to extend the fitting range of the model to smaller q-values the bubble correlation effects have to be included. This means that the interference of the scattering from different bubbles should be included in the scattering cross section. We have used the local monodisperse approximation (Pedersen 1994) for spheres with hard-sphere interactions:

$$\frac{\mathrm{d}\sigma}{\mathrm{d}\Omega}(q) = \Delta\rho^2 \int_0^\infty \Phi(q, R)^2 S(q, R)\, N(R)\ \mathrm{d}R \tag{16}$$

where $S(q, R)$ is the structure factor, which we take as the one calculated in the Percus–Yevick approximation (Pedersen 1994). The structure factor depends on the hard-sphere

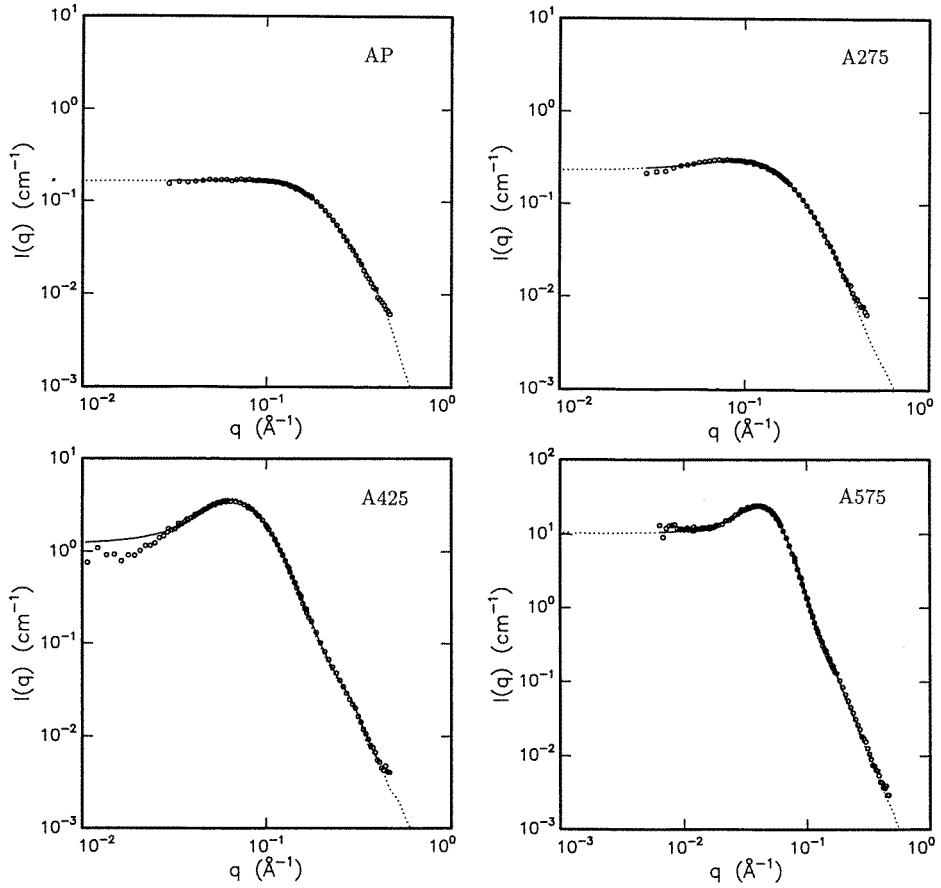

Figure 4. Small-angle scattering from the bubbles with the power-law scattering at low q and double Bragg scattering subtracted. The curves are fits with the local monodisperse model.

interaction radius R_{HS} and the volume fraction η of the hard spheres. We take R_{HS} to be proportional to the radius R, and we take the volume fraction η to be the same for all interaction radii. In the least-squares fit of the cross section to the experimental data, the proportionality constant R_{HS}/R and the volume fraction η of the hard spheres are free fitting parameters. The size distribution is again expressed as a linear combination of cubic b-splines and the fitting parameters determined as described by Pedersen (1994). It should be noted that (16) is only approximate and therefore R_{HS}/R and η should be considered as effective parameters describing the inter-particle interference effects.

The model fits the data (figure 4) for the samples AP, A275, and A575 very well with MSR = 2.3, 3.5, and 6.0, respectively. However, for the A425 sample the model fails at low q, where the measured intensity is lower than the optimized model intensities. This region is sensitive to the subtraction of the power-law scattering at low q from the originally measured data.

The size distributions (figure 5) are close to those determined when only the high-q part of the data is fitted. For the AP and A275 samples the size distributions are smoother than those determined from fitting only the high-q part of the data. The oscillations at large

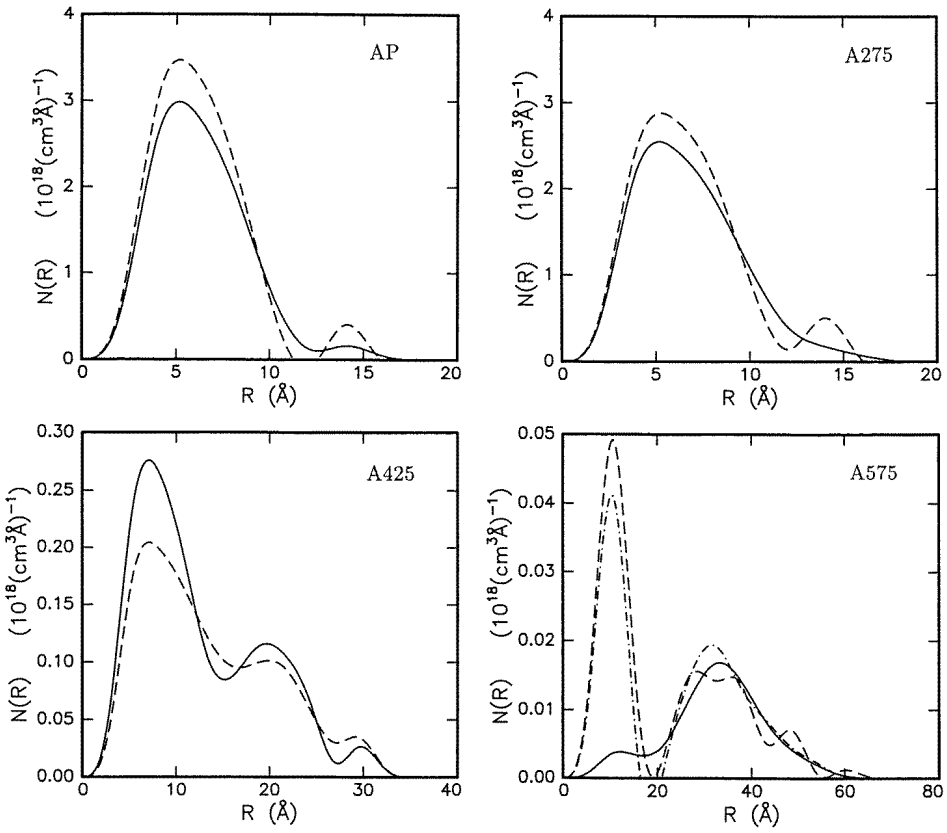

Figure 5. Size distributions. The broken curves are from fitting only the high-q part of the data assuming spherical bubbles. The full curves are from the local monodisperse model. For A575 the bubbles with radii larger than 40 Å are assumed to be octahedra. The chain curve for A575 is from assuming a spherical shape of all bubbles.

R-values have disappeared due to a better description of the data in the low-q part where the effects of bubble–bubble correlations are important. The size distribution for the A575 sample has a large component of small bubbles and it displays some oscillatory behaviour. As mentioned previously, the larger bubbles are faceted at this temperature. Therefore we also fitted the data using the form factor of an octahedron for the larger bubbles. The orientationally averaged form factor was calculated from the expressions given by Hendricks *et al* (1974). For comparisons with the size distributions of the spheres, a radius-equivalent size of an octahedron was defined as the radius of a sphere with the same volume. The limit between the spheres and the octahedra in the size distribution was varied and it was found that if bubbles with $R > 40$ Å were octahedra, the component of the size distribution centred at around 10 Å would almost disappear. This limit is in fair agreement with the observations by TEM (section 4).

The parameters derived from the size distribution are given in table 4 and plotted in figure 6. The values are nearly identical to those calculated from the size distributions determined only from the high-q part of the data. The main difference is a slightly larger average radius R_{Av} for the AP and A275 samples. The values estimated for the volume

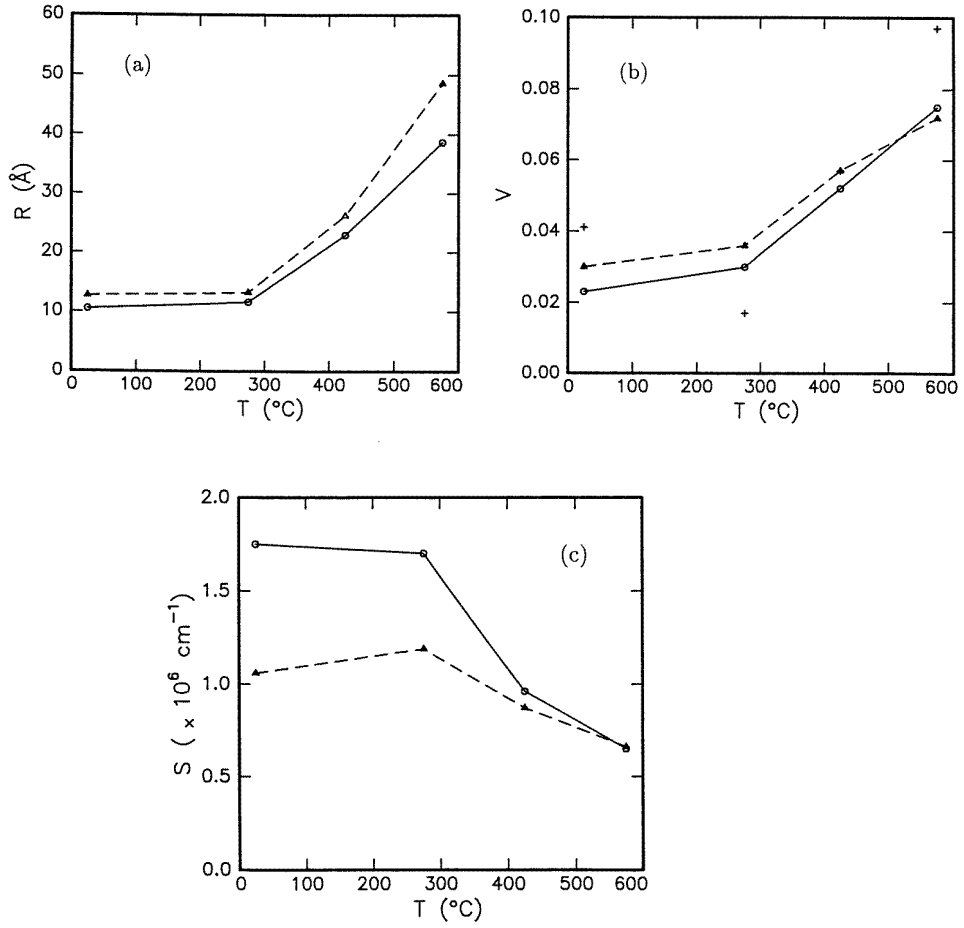

Figure 6. Results from the local monodisperse model compared to other models. (a) Bubble radii. Triangles: the average (weighted according to (15)) radius derived from the size distributions from the local monodisperse model. Circles: the radius of the bubbles from the two-shell model. (b) Volume fractions. Triangles: calculated from the size distribution. Crosses: from η and R_{HS}/R, both in the local monodisperse model. Circles: the two-phase model. (c) Specific surface area. Triangles: from the size distribution. Circles: from fit of the Porod expression.

fraction $V = \eta(R/R_{HS})^3$ are also given in table 4. For the A275 sample the value is about a factor of two smaller than the values determined from the size distributions. For the other three measurements there is a reasonable agreement.

The inclusion of the bubble correlation effects in the data analysis in the local monodisperse approximation is rather crude. It should be expected that the expressions given by Vrij (1979) which more correctly combine the effects of polydispersity and the interaction through the hard-spheres potential would work better. A program that applies a non-linear least-squares procedure to the model given by Vrij (1979) was written (Pedersen 1994). The size distribution was again parametrized as a sum of cubic *b*-spline functions. Surprisingly, the program failed to fit the experimental data although it worked reliably on simulated data. In the fit the parameters in the model were extremely correlated which

prevented a reliable optimization. For the best fits that we obtained, the MSR values were significantly larger than for the local monodisperse model. The model assumes complete randomness in the spatial distribution of the bubbles and also that the interaction radius R_{HS} is strictly proportional to the radius R. It can be either, or both, of these assumptions which are poorly justified.

4. Transmission electron microscopy: results

4.1. General microstructure

The general microstructural features present in the as-prepared specimens, as well as the annealed specimens have been described earlier (Eldrup and Evans 1982, Evans *et al* 1985, Jensen *et al* 1988). These observations, which are confirmed by the present study, may be summarized as follows. The as-prepared material is dominated by a very high density of small, spherical bubbles with diameters in the range up to 30 Å. In addition, the average grain size was very small, of the order of a few tenths of a micrometre, and the substructure showed a high density of dislocations.

Specimens which were prepared from slices taken parallel, and perpendicular to the deposition layers were entirely comparable; no heterogeneity could be seen by TEM even though macroscopic inspection (optical microscopy, $\times 50$) showed a structure which had clear fluctuations of alternating dark and light layers.

The microstructures following annealing showed some grain boundary migration, and a reduction in dislocation density as well as a coarsening of the krypton bubbles. The structure remained, however, rather homogeneous; in particular, no large bubbles were observed near grain boundaries, as had been reported earlier for, e.g., He-implanted Ni (Marochov *et al* 1987, Qiang-Li *et al* 1990).

4.2. Quantitative TEM of krypton bubbles

The krypton bubbles could be successfully imaged both in 'weak-beam' dark-field micrographs and using 'cavity contrast'. In the as-prepared material (AP), as well as in A275 the bubbles appeared spherical. Some faceting of the larger bubbles was observed in A425 and the majority of bubbles were clearly faceted in A575.

Table 5. Comparison of SANS, TEM, PAS and MDM results. The SANS results are from the polydisperse model which includes the inter-particle correlation effects in the local monodisperse approximation. The TEM results are calculated from the corrected size distributions. The average radius $\langle R \rangle$ is the centre of mass of the size distribution. For the PAS and MDM measurements V is calculated from the Kr density in the bubbles and the sample mass density, respectively.

	Radii		Volume fractions			
	$\langle R \rangle$ (SANS) (Å)	$\langle R \rangle$ (TEM) (Å)	V(SANS)	V(TEM)	V(PAS)	V(MDM)
AP	6.3	5.6	0.030	0.045	0.079	0.078
A275	6.8	7.9	0.036	0.065	0.081	0.063
A425	12.5	12.0	0.057	0.079	0.102	0.100
A575	33.0	25.9	0.072	0.071	0.128	0.125

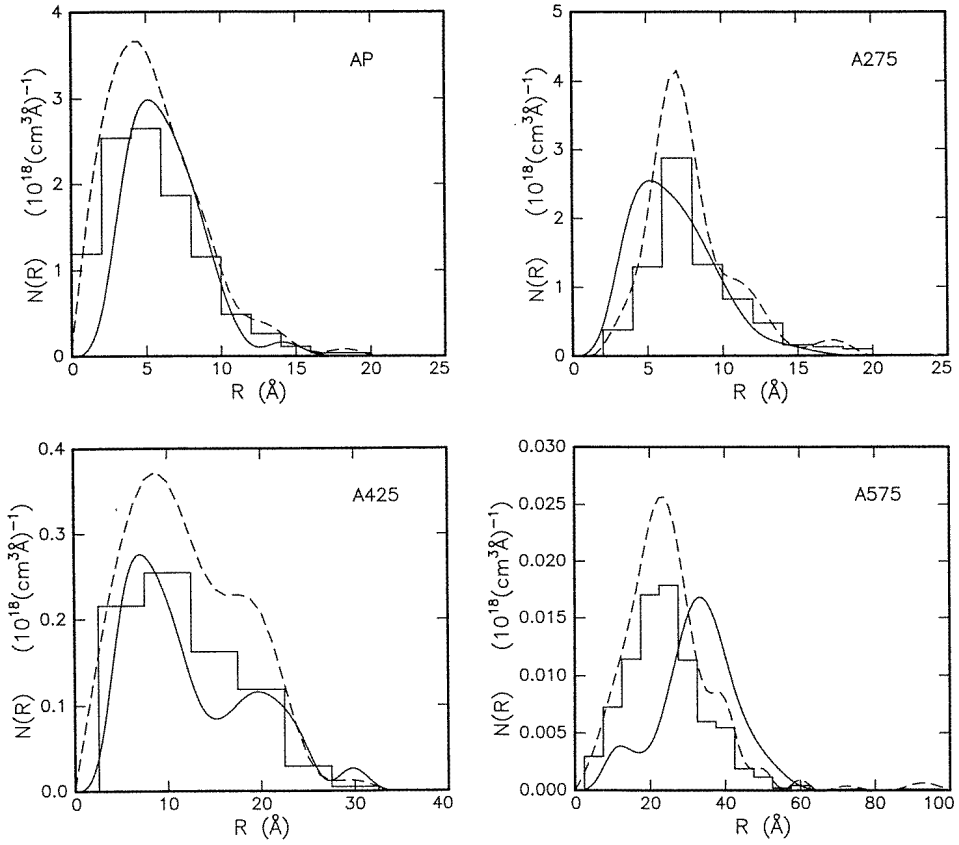

Figure 7. Size distributions. The full curves are from SANS using the local monodisperse model. The histograms are the observed and the dashed curves are the corrected distributions from TEM.

Due to the small size of the bubbles, there were considerable problems in achieving sufficient contrast from small bubbles, and due to the high densities of bubbles, there were major difficulties with image overlap, such that many of the bubbles were obscured. Both to improve bubble contrast and to reduce image overlap, it was therefore necessary to observe the bubble population in extremely thin regions of the foil (∼100 Å). These thin foils were however found to suffer from 'etching-out' of those bubbles which touched the foil surface during electro-polishing. Bubbles that had 'etched-out' typically gave surface pits which were faceted and clearly larger than the population of krypton bubbles. These surface pits were therefore relatively easy to recognize but were not included in the numbers of bubbles counted since it was not possible to determine the original sizes of the bubbles. The number of krypton bubbles which were 'lost' was found to be significant, particularly for the case of larger average bubble sizes in very thin foils. Image overlap is reduced as much as possible during observation in the electron microscope by selecting areas of the foil which are as thin as possible. However, for very high densities of small bubbles some image overlap is unavoidable and an overlap correction is required. This problem has been treated in detail by Kirkegaard *et al* (1996). They devised a correction procedure that includes the effect of

bubble etching-out at the surface as well as the effects of bubble images hiding or partly overlapping the images of other bubbles.

The results from TEM as expressed by the corrected values of mean bubble radius and swelling are given in table 5. The observed and corrected size distributions are given in figure 7.

5. Other measurements: results

Apart from the SANS and TEM studies described above some positron annihilation lifetime spectroscopy (PAS) measurements were made on samples cut from the same Cu(Kr) specimen as used for SANS and TEM. Furthermore, mass-density measurements were made as discussed below.

The PAS studies were made primarily to ascertain that the annealing behaviour of the present samples was the same as that observed by Jensen *et al* (1988). This was confirmed. A long-lifetime component due to positrons trapped in microscopic and submicroscopic Kr bubbles is observed. The value of this lifetime is a measure of the average Kr density, n_{Kr}, in the bubbles (Jensen and Nieminen 1987). The total cavity volume in the sample can be estimated from the average Kr density using the relation $V = (n/n_{Kr})G$, where n is the Cu-atom density in the matrix and G is the total Kr content (Jensen *et al* 1988). If the Kr density in the bubbles varies with bubble size, the Kr density derived from the long positron lifetime may deviate somewhat from the average density in the bubbles. However, a realistic estimate is that the average Kr density in the bubbles will be overestimated by only about 4% for a size distribution similar to the ones found by SANS (figure 5). The effect is therefore smaller than the uncertainties associated with the determination of n_{Kr} from PAS.

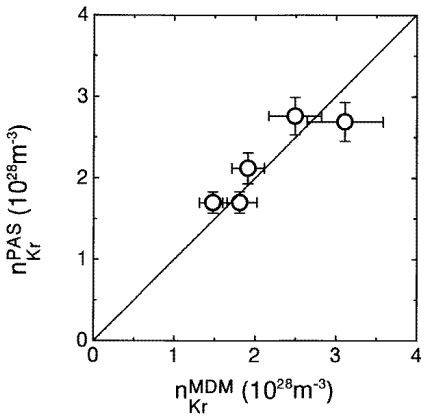

Figure 8. The average Kr density in cavities as derived from mass-density measurements (n_{Kr}^{MDM}) and PAS (n_{Kr}^{PAS}). The PAS densities of the bubbles do not include possible small vacancy–Kr clusters. The error bars arise from uncertainties in measurements of sample weight and dimensions (horizontal) and from estimated uncertainties in the PAS experiments (vertical).

Another, very simple way to determine the cavity volume V and average Kr density in the cavities, n_{Kr}, is to derive them from a measurement of the sample mass density. Because of the high Kr content, the values can be obtained with reasonable accuracy (Evans *et al* 1985). In the present case the density was determined by measurements of dimensions and

weights of a sample cut as a rectangular parallelepiped. The as-prepared sample was also annealed to 275, 425 and 575 °C, and density and PAS measurements carried out after each annealing treatment. The gas content was determined from the weight loss after a final anneal to 800 °C. The values of V obtained from the PAS and mass density are given in table 5, and figure 8 shows a comparison of the derived average Kr densities in the cavities. Typically, n_{Kr} varies from about 3 to 1.5 (10^{22} cm^{-3}) from AP to A575 (equivalent to a vacancy to Kr ratio of 2.8 and 5.6, respectively).

6. Discussion

The discussion in this section will be divided into three parts. First we consider the results obtained by the analysis of the SANS data, with the purpose of comparing the different approaches used in the analyses. Secondly we compare the SANS data to the results obtained by TEM, PAS and MDM, and finally we discuss the annealing behaviour of the Kr bubbles in Cu on the basis of these results and with reference to previous studies of this material.

6.1. Analysis of SANS data

In this subsection we compare the results obtained from the different SANS analyses, namely from (1) the 'model-independent' ('two-phase') analysis, (2) the monodisperse ('two-shell' and 'hard-sphere') models, and (3) the polydisperse models (without and with bubble correlation effects included).

The volume fraction V of the Kr bubbles is a parameter which was obtained both from a 'model-independent' approach (the two-phase model) and from the monodisperse and polydisperse models (see tables 1 and 4). In general, there is good agreement between the values obtained by the various approaches (about 20% deviation or less), with the trend that the polydisperse models give higher values than both the monodisperse and the two-phase models. This is in line with the expectation that fits of monodisperse models to data for a polydisperse system will give rise to some systematic errors in the fitted parameters, and with the results of analysis of simulated data for a polydisperse hard-spheres system by a monodisperse hard-sphere model. Such investigations have shown that the volume fractions determined were too small (Pedersen 1993b).

The specific surface area S was estimated in two ways, namely by fitting the Porod expression (5) to the data at large q, as well as being calculated from the size distributions obtained from the polydisperse models (12). The Porod expression gives much larger values of S for the samples AP and A275, whereas the values from the two approaches agree within 10% for the samples A425 and A575. As mentioned in section 3.3.1, the discrepancies for the AP and A275 samples are due to the application of the Porod expression outside its range of validity and we can conclude that the Porod expression should be used with caution for the determination of surface areas. When using the polydisperse models, one fits a weighted form factor to the data. This gives rise to constraints in the model as it has to fit the full range of scattering vectors ranging from the 'Guinier' region to the Porod region, and this ensures correct interpretation of the data.

The bubble radii obtained from the monodisperse models (tables 2 and 3) are in close agreement, but systematically smaller than the average radii (15) obtained from the polydisperse model that includes particle correlation effects (table 4). A final comparison concerns the size distributions determined by the two polydisperse models, i.e. without and with the inclusion of the inter-particle correlation effects. It can be seen in figure 5 that the

distributions from the model that includes correlation effects are generally smoother. Also the distributions from TEM are relatively smooth, and we conclude that the inclusion of the inter-particle correlation effects in the local monodisperse approximation eliminates artificial oscillations in the size distributions. It should also be noted that the size distributions obtained from the SANS data are very sensitive to the assumed form factor of the particles (section 3.3.2).

Important sources of error in the size distribution from the SANS experiments are the determination of the absolute scale of the intensity in the scattering experiment and the determination of the contrast $\Delta\rho^2$. Errors on both of these give rise to an error on the absolute concentration of bubbles and thus on the parameters S and V derived from the size distribution. Comparisons with the scattering from a single crystal of vanadium show that the uncertainty on the normalization which is based on the scattering from water is less that 5% (Vyskocil *et al* 1992). The relative uncertainty on the contrast $\Delta\rho^2$ is, in the present case, roughly equal to the relative uncertainty on the Kr density in the bubbles. We estimate this to be about 25%, which gives a total uncertainty on the amplitude of the size distribution of 25%.

6.2. Comparison of SANS, TEM, PAS and MDM results

The most direct comparison of the results obtained from SANS and TEM is shown by the plots of the size distributions in figure 7. The shapes of the size distributions are in fairly good agreement, but the SANS distributions generally indicate lower bubble densities than the TEM distributions. However, with the 25% uncertainty in the amplitudes of the SANS distributions mentioned above and a similar (or probably larger) uncertainty on the TEM data, this difference is probably not significant and therefore does not reflect any systematic error in the measurements (see further below).

The distributions for the A425 sample are clearly qualitatively different from the other distributions. The latter are rather narrow, while the A425 ones are rather broad. Both the SANS and TEM results give evidence of a bimodal distribution. A similar broad, perhaps bimodal distribution was reported by Williamson (1985) in TEM studies of similar material annealed to 450 °C. The agreement between the SANS and TEM distributions is also illustrated by the agreement of the values for the average (first-order-moment) radius $\langle R\rangle$ listed in table 5.

Estimates of the volume fraction V of the bubbles are given in table 5. As a consequence of the good agreement between the krypton densities in the bubbles as estimated by PAS and MDM (figure 8), the bubble volume fractions derived from these two techniques show good agreement. Since simple measurements and calculations involving essentially no assumptions lead to the MDM values of V, we may reasonably assume V(MDM) to be the best estimate of the total cavity volume. Although the general trend of an increasing bubble volume fraction at the higher temperatures is the same for all four derivations of V, it is surprising that V(SANS) generally is only about half of V(MDM). This difference apparently cannot be accounted for in terms of experimental uncertainties on the volume fractions, since the best estimate for SANS is about 30% uncertainty on V. It should be noted though, that if large variations of Kr density with bubble size were present, additional systematic errors might occur. An additional uncertainty might be that small Kr–vacancy clusters (with a radius of 1–3 Å) are not observed due to the resolution of the experiment. If the presence of such clusters were taken into account in the analysis, it would lead to a small reduction of the contrast factor $\Delta\rho$, and thus result in slightly larger volume fractions.

Although the uncertainties on the values of V(TEM) probably are bigger than those

for V(SANS), the TEM results also seem to be systematically lower than V(MDM) and V(PAS). Accepting this difference between the Vs derived from size distributions on the one hand and those based on average krypton densities on the other, we are led to suggest (in agreement with earlier work, e.g. Jensen *et al* 1988) that an appreciable part of the cavity volume is not detected by SANS and TEM. The present study shows that this is true even after annealing to 575 °C. Furthermore, since the krypton density in the microscopic and submicroscopic bubbles as detected by PAS equals the average krypton density in the total cavity volume, it seems likely that the cavities not seen by SANS and TEM similarly contain an appreciable fraction of the total krypton inventory in the samples. As mentioned above, there is good evidence from SANS and PAS that at the lower annealing temperatures there exists a population of small vacancy clusters which cannot be seen in TEM and are only indirectly detected by SANS (i.e. they do not show up in the derived cavity size distribution, but are seen as a change of the matrix scattering length density during annealing). These clusters may contribute a significant fraction of the cavity volume that is not seen by TEM or SANS. However, at the higher annealing temperatures these small clusters apparently disappear, so the 'missing cavity volume' and Kr must be found elsewhere. Maybe grain boundaries contain Kr-stabilized cavities that could account for this. Because of the very small grain size, the volume associated with 5 Å wide grain boundaries amounts to roughly 1%. Williamson (1985) and Evans *et al* (1985) observed diffusion of gas to, and large bubbles at, the grain boundaries as precursors for the strong gas release observed above the present annealing range. Large bubbles at grain boundaries may not have been detected by the present TEM and SANS measurements.

6.3. Annealing behaviour

The results from SANS and TEM show an onset of bubble growth at around 300 °C in agreement with the results from PAS (Jensen *et al* (1988) and measurements on the present samples) as evident from the increase in bubble radius shown in figures 2, 5–7 and tables 2–5. In addition, the data from all of the techniques show an increase in the bubble volume fraction V and a decrease in the specific surface area S beginning at about this temperature (see e.g. table 4 and figure 6). One also observes the largest changes in the parameters related to the inter-particle interference effects in the SANS data between 275 °C and 425 °C as seen by the appearance of the peak in the scattering curve (figure 1) and the clear structure in the distance distribution function above the self-correlation peak (figure 2). Similarly, in the two-shell model the ratio between the scattering densities in the two shells shows a strong change at around 300 °C (table 2).

In the following, we first discuss the annealing behaviour at the higher temperatures, i.e. above 0.5 T_m (where T_m is the melting temperature, 405 °C in Cu), before we return to the temperatures below 0.5 T_m. Bubbles of the heavier rare gases are normally believed to grow by the so-called migration and coalescence processes by which each bubble diffuses in a Brownian fashion and, when encountering another bubble, coalesces with it. In this way the average bubble size grows while the density decreases. Furthermore, at temperatures above approximately 0.5 T_m the concentration of thermal vacancies and their diffusivity is high enough to permit overpressurized bubbles to absorb vacancies, and in this way to increase the total bubble volume. Since the surface diffusion of matrix atoms at the gas matrix interface normally has the lowest activation enthalpy of the possible diffusion paths, the bubble migration rate will be controlled by the surface diffusion (Goodhew and Tyler 1981, Donnelly and Evans 1991), although if the surface diffusion is impeded, e.g. by the presence of impurities at the bubble surface, volume diffusion may also apparently

play a role (Yamaguchi *et al* 1989, Cox *et al* 1989). Other bubble migration mechanisms, e.g. diffusion through the gas of metal atoms (Goodhew and Tyler 1981, Trinkaus 1989), or Ostwald ripening (by which gas–vacancy complexes would dissociate from smaller bubbles and agglomerate with bigger ones) are less likely mechanisms for bubble growth. For a big atom like Kr, the activation energy for dissociation may be several electron volts (Melius *et al* 1980, Trinkaus 1989), and Ostwald ripening would not take place at temperatures as low as 0.5 T_m. The high gas concentration (about 2.6 at.%) would also tend to favour the migration and coalescence mechanism rather than Ostwald ripening (Schroeder *et al* 1991, Goodhew 1991).

We can make a very rough estimate of the apparent activation energy, E_a, for the growth of bubble radius with temperature, using the SANS and TEM data above 0.5 T_m (table 5), and find $E_a = 0.25 \pm 0.07$ eV. If the radius increase is due to migration and coalescence of bubbles the activation energy of the rate-determining diffusion process, Q, should be 4–6 times E_a, depending on the actual process (volume or surface diffusion) and on whether the bubbles are in equilibrium or have a constant gas density (Goodhew and Tyler 1981). Thus, in our case, Q would be in the range 0.7–1.9 eV, a range covering an expected activation energy for surface diffusion of roughly 1 eV (Evans and van Veen 1989) (and also being close to the self-diffusion activation energy for copper of 2.19 eV (Fujikawa and Hirano 1982)). If the increase in radius were, on the other hand, determined by ripening, Q should be 2–3 times E_a (Goodhew and Tyler 1981, Trinkaus 1989), i.e. 0.35–1.0 eV. This range is much lower than the expected values for the effective dissociation energies of vacancies and Kr atoms from bubbles (Trinkaus 1989). Thus, we interpret the growth of bubble size and bubble volume fraction at 425 °C and 575 °C as due to migration and coalescence of bubbles followed by absorption of thermal vacancies. It is not clear whether the bubbles absorb enough vacancies to reach thermal equilibrium, because the uncertainties in the derived Kr densities and hence in the pressure lead to rather large uncertainties in calculations of equilibrium bubble radii.

It is perhaps more interesting to consider the annealing behaviour between 275 °C and 425 °C, i.e. mainly below 0.5 T_m: the lifetime of positrons trapped in Kr bubbles is constant up to 300 °C (0.42 T_m) (Jensen *et al* (1988) and present PAS measurements). Since the positron lifetime is correlated with the Kr density in the bubbles (Jensen and Nieminen 1987) this shows that the average Kr density in the bubbles starts to decrease (i.e. the bubble volume starts to increase) at about 300 °C. This is in agreement with the present SANS and TEM measurements that show no (or very little) change in the bubble population at 275 °C, but a clear increase in bubble volume fraction at 425 °C. In the following we consider two aspects of this. One is the question of what initiates the bubble growth, while the second one concerns the mechanism by which the bubble volume growth takes place below 0.5 T_m, where the concentration of thermal vacancies is low. These questions were also the subject of discussions by Jensen *et al* (1988), but the present measurements add some new aspects.

In the following we shall discuss two different mechanisms that may be responsible for the initiation of bubble growth. By the first mechanism, melting of Kr in the largest bubbles allows these bubbles to migrate and coalesce with smaller bubbles and clusters. By the second, submicroscopic vacancy clusters containing Kr are assumed to start to migrate at about 300 °C and to coalesce with the bubbles.

Jensen *et al* (1988) suggested that up to about 300 °C, bubble movements were effectively prevented by the presence of solid krypton in the bubbles. On heating to about 300 °C the Kr melts (as seen by electron diffraction (Evans and Mazey 1985)) and surface diffusion and thereby bubble migration may take place. It is not unreasonable to expect

that the bigger bubbles have the lowest Kr density and pressure (Jensen *et al* 1988). If so, the bigger bubbles would then melt at the lowest temperatures and therefore be the first to migrate and coalesce with both bubbles and smaller clusters. Actually, the present SANS data suggest that the average Kr density in the matrix (i.e. in between those bubbles that are big enough to be resolved by SANS) is strongly reduced after annealing to 425 °C (section 3.2). Most of the Kr density in the matrix probably has to be associated with small vacancy clusters (too small to be resolved by SANS and TEM) containing Kr atoms (see further below), and a strong reduction of Kr density in the matrix therefore would be due to the coalescence of the migrating bubbles with many of these immobile clusters. The disappearance of small vacancy–Kr clusters at about 300 °C would also be in agreement with the PAS data (Jensen *et al* (1988) and the present results). Support for this mechanism is obtained from the size distribution for A425 which has a bimodal character (section 6.2 and figure 7). As discussed by Rest and Birtcher (1989) and Birtcher (1991) for bubbles generated by Kr implantation in Ni, a bimodal distribution may evolve, either during the implantation or during subsequent annealing, provided that the temperature is so high that the krypton in some of the bubbles (the bigger ones) is fluid, while in some (the smaller ones) it is solid. They concluded that under these conditions the bigger bubbles may migrate and coalesce with other bubbles and therefore grow, while the smaller, solid bubbles will remain immobile. Those of the small bubbles that do not coalesce with the moving big bubbles do not change size. In this way a bimodal distribution develops. The bubble growth observed in the present work can apparently be understood along the same lines.

The second mechanism that we shall consider which may initiate the bubble growth at about 300 °C is one where the small Kr–vacancy clusters become mobile at this temperature. The decrease of the density of small vacancy–Kr clusters at about 300 °C, of course, need not be caused by migrating bubbles coalescing with the clusters which was the process discussed above. The other possibility is that the clusters themselves start to migrate at this temperature. This interpretation is supported by the work of Yagi (1989, 1991) and Kuzminov *et al* (1992). Yagi uses channelling experiments to obtain information about the lattice location of Kr atoms implanted at room temperature in aluminium and finds evidence for the presence of both small clusters (KrV_n with $n = 1$–6) and bubbles. On annealing to about 0.65 T_m the fraction of Kr atoms in the small clusters decreases while the fraction in bubbles increases. Kuzminov *et al* implanted copper with Kr ions at room temperature and subsequently annealed at 0.45 T_m. In the as-implanted specimens, no bubbles could be observed (except at the highest doses) by TEM or electron diffraction, but after annealing solid bubbles were seen to be present, thus giving evidence for the migration of clusters at 620 K. Although the implantation conditions in the experiments of Yagi (1989) and Kuzminov *et al* (1992) are different from those used to produce the present samples (higher ion implantation energy, lower total Kr density and implantation into bulk metal from one surface) their results support the suggestion that migration of small clusters does take place below 0.5 T_m in the present samples. This would also agree with the estimated upper limit of the migration energy of a KrV_2 complex (albeit in Ni) of 1.8 eV (Melius *et al* 1980) which is equivalent to a migration temperature of about 0.45 T_m. Complexes with one or two more vacancies are likely to migrate at about the same or slightly lower temperatures.

If we accept this migration of small clusters and assume for the moment (an assumption to be discussed below) that the average vacancy-to-Kr ratio in the migrating clusters is higher than the ratio of about 3 determined for the bubbles in AP and A275 (section 5), it is easy to understand that when the clusters coalesce with bubbles, not only does the average bubble size increase, but the Kr density in the bubbles decreases, in agreement with observations. This would also tend to release the overpressure in the bubbles in the

as-prepared specimens. Evidence for the existence of such an overpressure comes from the expansion of the Cu lattice in the as-prepared samples (Williamson 1985). The Cu lattice parameter relaxes to the normal value for bulk Cu in a range from about 250 °C to 400 °C, consistent with the above suggestion.

A reduction in Kr density may lead to melting of the solid Kr. Thus the observed melting (Evans and Mazey 1985) may be a result not only of the increase in temperature, but also of pressure release in the bubbles due to coalescence with migrating small clusters. The rate with which the diffusing clusters will coalesce with bubbles of radius R will be approximately proportional to R. Thus, if submicroscopic clusters diffuse and coalesce with a population of bubbles, the relative change of the volume of a bubble of radius R will on average be proportional to $1/R^2$. Therefore, the change in Kr density will be largest for the small bubbles and thus the small bubbles may be the first to melt, contrary to the mechanism discussed earlier. Once melted, the bubbles may migrate and coalesce as discussed above. However, it is maybe more difficult to see how a bimodal size distribution can develop if the small bubbles melt first.

Let us briefly return to the assumption made above, namely that in the smallest Kr_mV_n clusters, the ratio n/m is bigger than the average for the bubbles ($\approx$3). An indication of this is given in the work by Yagi (1989) on Kr-implanted Al, for which he derives, at low doses, that clusters containing one Kr atom may contain up to 6 vacancies (on average 3.3). In the work on Kr-implanted Cu, Kuzminov *et al* (1992) found that, with increasing Kr dose, the V/Kr ratio decreased from $\approx$3.5 to $\approx$3.0; this effect was associated with increasing recombination of vacancies and interstitials at the higher doses, due to cascade overlap. Thus, in a small cluster formed during relaxation of a cascade, it is not unreasonable to expect the V/Kr ratio on average to be about 3.5 or higher.

Finally, we should mention that Jensen *et al* (1988) proposed that loop punching might be responsible for the initiation of bubble growth. However, it seems that in general the pressure in the bubbles (2–4 GPa) is not high enough for loop punching to operate, since about 10 GPa would be necessary for bubbles with radii of about 10 Å (Donnelly *et al* 1991, Trinkaus 1991), although it probably cannot be excluded that a small fraction of the bubbles may be large enough or their pressure big enough for the loop punching to operate.

7. Summary and conclusions

In the present work we have studied the annealing behaviour of Cu containing a high density of Kr bubbles using small-angle neutron scattering (SANS), transmission electron microscopy (TEM) supplemented with data from positron annihilation spectroscopy (PAS) and mass-density measurements (MDM). In order to make as direct a comparison as possible between the information obtained from the various techniques, specimens for all of the measurements were cut from the same piece of material. The present investigation is a continuation of earlier studies on similar material but now with the important addition of the SANS technique. Special emphasis was therefore put on the discussion of different approaches to the analysis of the SANS data.

We conclude from the comparison of the different types of SANS data analysis that the polydisperse models clearly give the most extensive information as they give both the size distribution and the integral parameters (V, S, and R_{Av}) derived from it. However, it was seen from the analysis for the A575 sample that the reliability of the size distribution depends critically on the correct form factors being used. This is particularly important when the data are recorded for a large range of scattering vectors, so that both the 'Guinier' part ($q < 1/R_{Av}$) and the 'Porod' part ($q \gg 1/R_{Av}$) of the scattering curve are probed. The

most reliable results that can be derived from the SANS data are those obtained from the model which includes the inter-particle correlation effects. For the samples studied in the present work this model is also the one that agrees best with the microstructure observed by TEM.

Because of a very high density of bubbles in the specimens, TEM micrographs showed appreciable overlap of bubble images. In order to obtain the undisturbed bubble size distribution from the TEM data, a new correction procedure for bubble overlap and bubble disappearance at the specimen surfaces was developed (published separately (Kirkegaard *et al* 1996)). The shapes of the resulting TEM size distributions agreed well with the equivalent ones from SANS, although the amplitudes of the SANS distributions were up to 30% lower than the TEM ones. This difference was estimated to be within experimental uncertainty. On the other hand, estimates of the total cavity volumes gave significantly lower values for TEM and SANS than were obtained from PAS and MDM. This discrepancy was tentatively ascribed to the presence of large volume cavities in grain boundaries and, at the lower annealing temperatures, to the presence of submicroscopic vacancy–krypton clusters. We want to note that in the present work, it has been useful to combine different experimental techniques. The partly complementary techniques have provided insight into the shortcomings and strengths of the different techniques.

In agreement with earlier studies, the Kr bubbles were found to grow in size for annealing temperatures above approximately 300 °C. Two possible mechanisms for the initiation of bubble growth were discussed: one where it is the melting of solid Kr in the largest bubbles that allows migration and coalescence to start, and one where the migration of small Kr–vacancy clusters leads to the initial growth of bubbles. It has not been possible to provide clear evidence that could differentiate between these two mechanisms. However, the melting and migration of the largest bubbles provides a possible explanation for the observation of a bimodal distribution at 425 °C, and we are therefore more inclined to believe that this is the dominating process. In both cases, though, coalescence between bubbles and small clusters will be operating. A higher-than-average vacancy-to-Kr ratio in the small clusters was taken to provide a qualitative explanation of why the Kr density in the bubbles decreases even at temperatures below 0.5 T_m. Above 0.5 T_m the observed growth in bubble size and total volume fraction was explained by bubble migration and coalescence followed by absorption of thermal vacancies.

Acknowledgments

Stimulating discussions with Kell Mortensen, John Evans, Peter Kirkegaard, and Kjeld O Jensen are gratefully acknowledged. We thank John Evans for providing the samples and for comments on the manuscript, and Peter Kirkegaard for computations of the TEM corrections. Thanks are also due to Dorte Juul Jensen for a texture measurement and Jørgen Bilde-Sørensen for SEM investigations.

References

Abis S, Carciuffo R, Carsughi F, Coppola R, Magnani M, Rustichelli F and Stefanon M 1990 *Phys. Rev.* B **42** 2275

Baur R and Gerold V 1964 *Acta Metall.* **12** 1449

Birtcher R C 1991 *Fundamental Aspects of Inert Gases in Solids* ed S E Donnelly and J H Evans (New York: Plenum) p 133

Cox R J, Goodhew P J and Evans J H 1989 *Nucl. Instrum. Methods* B **42** 224

Donnelly S E 1985 *Radiat. Eff.* **90** 1

Donnelly S E and Evans J H (ed) 1991 *Fundamental Aspects of Inert Gases in Solids* (New York: Plenum)
Donnelly S E, Mitchell D R G and van Veen A 1991 *Fundamental Aspects of Inert Gases in Solids* ed S E Donnelly and J H Evans (New York: Plenum) p 357
Eldrup M and Evans J H 1982 *J. Phys. F: Met. Phys.* **12** 1265
Evans J H and Mazey D J 1985 *J. Phys. F: Met. Phys.* **15** L1
Evans J H and van Veen A 1989 *J. Nucl. Mater.* **168** 12
Evans J H, Williamson R and Whitmell D S 1985 *Effects of Radiation on Materials: 12th Int. Symp. (STP 870)* ed F A Garner and J S Perrin (Philadelphia, PA: American Society for Testing and Materials) p 1225
Fujikawa S and Hirano K 1982 *Point Defects and Defect Interactions in Metals* ed J-I Takamura, M Doyama and M Kiritani (Amsterdam: North-Holland) p 554
Glatter O 1977 *J. Appl. Crystallogr.* **10** 415
——1979 *J. Appl. Crystallogr.* **12** 166
——1980 *J. Appl. Crystallogr.* **13** 7
——1981 *J. Appl. Crystallogr.* **14** 101
Goodhew P J 1991 *Fundamental Aspects of Inert Gases in Solids* ed S E Donnelly and J H Evans (New York: Plenum) p 349
Goodhew P J and Tyler S K 1981 *Proc. R. Soc.* A **377** 151
Guinier A and Fournet G 1955 *Small-Angle Scattering of X-rays* (New York: Wiley)
Hendricks R W, Schelten J and Schmatz W 1974 *Phil. Mag.* **30** 819
Jensen K O, Eldrup M, Pedersen N J and Evans J H 1988 *J. Phys. F: Met. Phys.* **18** 1703
Jensen K O and Nieminen R M 1987 *Phys. Rev.* B **36** 8219
Juul Jensen D, Lorentzen T, Pedersen J S and Clausen K N 1992 *Proc. 2nd European Conf. on Advanced Materials and Processes* vol 3, ed T W Clyne and P J Withers (London: Institute of Materials) p 420
Kirkegaard P, Eldrup M, Horsewell A and Pedersen J S 1996 *Report* Risø-R-789(EN), to be published
Kuzminov D, Templier C, Raqi E and Garem H 1992 *Nucl. Instrum. Methods* B **62** 469
Laslaz, G, Kostorz G, Roth M, Guyot P and Stewart R J 1977 *Phys. Status Solidi* a **41** 577
Lebech B 1990 *Neutron News* **2** 7
Marochov N, Perryman L J and Goodhew P J 1987 *J. Nucl. Mater.* **149** 296
Melius C F, Wilson W D and Bisson C L 1980 *Radiat. Eff.* **53** 111
Pedersen J S 1993a *J. Physique Coll.* IV **3** C8 491
——1993b *Phys. Rev.* B **47** 657
——1994 *J. Appl. Crystallogr.* **27** 595
Pedersen J S, Posselt D and Mortensen K 1990 *J. Appl. Crystallogr.* **23** 321
Porod G 1982 *Small Angle X-ray Scattering* ed O Glatter and O Kratky (London: Academic)
Qiang-Li, Kesternich W, Schroeder H, Schwahn D and Ullmaier H 1990 *Acta Metall. Mater.* **38** 2383
Rest J and Birtcher R C 1989 *J. Nucl. Mater.* **168** 312
Schroeder H, Fichtner P F P and Trinkaus H 1991 *Fundamental Aspects of Inert Gases in Solids* ed S E Donnelly and J H Evans (New York: Plenum) p 289
Schwahn D, Ullmaier H, Schelten J and Kesternich W 1983 *Acta Metall.* **31** 2003
Trinkaus H 1989 *Scr. Metall.* **23** 1773
——1991 *Fundamental Aspects of Inert Gases in Solids* ed S E Donnelly and J H Evans (New York: Plenum) p 369
Ullmaier H (ed) 1983 *Proc. Int. Symp. on Fundamental Aspects of Helium in Metals; Radiat. Eff.* **78** 1
Vrij A 1979 *J. Chem. Phys.* **71** 3267
Vyskocil P, Sequeira A, Calderon H, Kostorz G and Pedersen J S 1992 unpublished
Warren B E 1959 *Acta Crystallogr.* **12** 837
Whitmell D S 1981 *Radiat. Eff.* **53** 209
Whitmell D S, Nelson R S, Smith K J S and Bauer G J 1983 *Eur. Appl. Res. Rep.–Nucl. Sci. Technol.* **5** 513
Wignall G D and Bates F S 1987 *J. Appl. Crystallogr.* **20** 28
Williamson R 1985 *Harwell Report* AERE-R 11273
Yagi E 1989 *Nucl. Instrum. Methods* B **39** 68
——1991 *Fundamental Aspects of Inert Gases in Solids* ed S E Donnelly and J H Evans (New York: Plenum) p 257
Yamaguchi H, Hashimoto I, Mitsuya H, Nakamura K, Yagi E and Iwaki M 1989 *J. Nucl. Mater.* **161** 164